A unified framework for personalized regions selection and functional relation modeling for early MCI identification

Jiyeon Lee [a,1], Wonjun Ko [a,1], Eunsong Kang [a], Heung-Il Suk [a,b,*], and the Alzheimer's Disease Neuroimaging Initiative[2]

[a] *Department of Brain and Cognitive Engineering, Korea University, Republic of Korea*
[b] *Department of Artificial Intelligence, Korea University, Republic of Korea*

ARTICLE INFO

ABSTRACT

Resting-state functional magnetic resonance imaging (rs-fMRI) has been widely adopted to investigate functional abnormalities in brain diseases. Rs-fMRI data is unsupervised in nature because the psychological and neurological labels are coarse-grained, and no accurate region-wise label is provided along with the complex co-activities of multiple regions. To the best of our knowledge, most studies regarding univariate group analysis or multivariate pattern recognition for brain disease identification have focused on discovering functional characteristics shared across subjects; however, they have paid less attention to individual properties of neural activities that result from different symptoms or degrees of abnormality. In this work, we propose a novel framework that can identify subjects with early-stage mild cognitive impairment (eMCI) and consider individual variability by learning functional relations from automatically selected regions of interest (ROIs) for each subject concurrently. In particular, we devise a deep neural network composed of a temporal embedding module, an ROI selection module, and a disease-identification module. Notably, the ROI selection module is equipped with a reinforcement learning mechanism so it adaptively selects ROIs to facilitate the learning of discriminative feature representations from a temporally embedded blood-oxygen-level-dependent signals. Furthermore, our method allows us to capture the functional relations of a subject-specific ROI subset through the use of a graph-based neural network. Our method considers individual characteristics for diagnosis, as opposed to most conventional methods that identify the same biomarkers across subjects within a group. Based on the ADNI cohort, we validate the effectiveness of our method by presenting the superior performance of our network in eMCI identification. Furthermore, we provide insightful neuroscientific interpretations by analyzing the regions selected for the eMCI classification.

1. Introduction

Mild cognitive impairment (MCI) is a symptomatic pre-dementia stage with a high risk of progressing to Alzheimer's disease (AD). Treatment of the early stage AD delays its progression; and as such, early detection of MCI has received significant attention for the improvement of treatment effectiveness. However, an early stages of MCI, with only subtle functional and structural changes is nearly undistinguishable from a normal condition in terms of cognitive function at the clinical level (Edmonds et al., 2019); this makes MCI diagnosis highly difficult. Additionally, even at the same clinical stage, heterogeneous symptoms such as cognitive deficits in memory, mild impairments in executive function,

or those in terms of processing speed (Delano-Wood et al., 2009) may exist. These symptoms may vary from one person to the other, and can be caused by a variety of risk factors such as gene and environment. Therefore, it is necessary to consider personalized biomarker anomalies to better understand the diverse neurophysiological patterns of MCI and perform accurate diagnosis.

Resting-state functional magnetic resonance imaging (rs-fMRI), which measures the low-frequency spontaneous fluctuations of blood-oxygen-level-dependent (BOLD) signals, is an emerging tool for discovering AD-related biomarkers with abnormal functional changes. In particular, several studies have attempted to classify subjects as AD/MCI patients or cognitively normal subjects based on the group representative functional characteristics of rs-fMRI. In these studies, feature extraction

and/or selection was first performed on the entire brain scale or regions of interest (ROIs) scale (Khazaee et al., 2017; Wee et al., 2014). In addition to being employed for dimensionality reduction because of the high dimensional nature of fMRI data, feature extraction and/or selection enables an intuitive analysis and yields better classification performance in the identification of subjects (Wang et al., 2013).

From the perspective of feature selection, previous studies (Chen et al., 2017; Wee et al., 2014) have used group-level statistical method, such as the *t*-test, which are applied to the ROIs for selecting task relevant features for classification. In this regard, other machine learning approaches (Qian et al., 2018; Wee et al., 2014) involve the use of a classifier with recursive feature elimination method based on the class-relevant weights of the classifier. Meanwhile, independent component analysis (ICA) has been widely utilized for analyzing intrinsic brain networks based on predefined group templates, such as the default mode network (DMN), control network, and somatomotor network, as biomarkers of brain diseases or disorders (Allen et al., 2011; Calhoun and Adali, 2012; Du et al., 2020).

Recently, deep learning (DL) has drawn attention in the domain of feature extraction as it enables the detection of informative brain activity features, which can be used to differentiate a patient from a normal in an end-to-end manner. Unlike traditional methods, DL allows for the extraction of features without prior knowledge and simultaneously learning of meaningful discriminative features for accurate diagnosis. For instance, Parisot et al. (2018) introduced a methodological framework to automatically learn a subject's relations with feature extraction based on functional connectivity (FC) has demonstrated the identification of a patient based on the population manner. Kawahara et al. (2017) devised a convolutional neural network (CNN) kernel for feature extraction suitable for learning functional networks. Furthermore, Dvornek et al. (2019) used a discriminative and generative network to learn neurological functional relations for disease classification. These statistical, machine learning, and deep learning-based feature selection and extraction approaches help in the identification of disease-related biomarkers and prediction of diseases with reliable classification rates.

One aspect that these methods have in common is that they are based on the assumption that; predefined diagnostic groups, i.e., the patient and normal groups, can be segregated from each other and have high homogeneity within each group (Du et al., 2018). Under this assumption, most existing studies have captured features that focus only on group differences. Specifically, an independent sample *t*-test assumes there is a statistical difference between the means of the two groups. In the meantime, machine learning and deep learning infer a function that maps the training fMRI dataset to a specific diagnostic group. However, in practice, symptoms and their level of severity differ from one patient to the other, even if all the patients are diagnosed with the same MCI status. Since early-stage mild cognitive impairment (eMCI) can develop into various types of dementia, individuals diagnosed with eMCI may show different disease-related regions from which dementia is highly likely to develop and with varying degrees of severity. Inconsistent brain activity patterns resulting from this discrepancy within a group might affect the discriminative power of the classification and result in inaccurate biomarker identification.

In this regard, the importance of individual biomarkers is emphasized (Arbabshirani et al., 2017; Rathore et al., 2017). Representative brain functional properties across subjects have provided meaningful insights into diseases in some cases. However, they may not be applicable to others (Mohr and Nagel, 2010; Mueller et al., 2013). Departing from the general approach, where the same significant ROI sets for all subjects are used for classification or analysis, it is necessary to consider individual variability by considering subject-specific diagnostic ROIs. However, it is challenging to cover both individual variability and common diagnostic group properties simultaneously because the rs-fMRI data contains complex signals, the psychological or neurological label is coarse-grained, accurate region-wise label is not available for the co-activities

of multiple regions, and a gold standard of disease-discriminative regions does not exist for each individual.

Hence, we devise a novel reinforcement learning (RL)-based approach to handle region selection individually without any prior knowledge. In the RL framework, the environment shows the agent a *state*; subsequently, the agent performs an *action* to maximize the total *reward* amount (Sutton and Barto, 2018). This action is reflected in the environment as well in the next state. Through an iterative interacting procedure, the agent finally achieves the maximal total reward through *trial-and-error*, even if the agent has no true label or prior knowledge. Deep-neural-network-based RL (deep RL), a method that applies DL to RL, is advantageous as it enables a fully autonomous agent without memory and computational problems, thereby addressing the limitations of traditional RL (Arulkumaran et al., 2017). Furthermore, a gradient, which is a learning signal from the neural network, helps in the effective approximation of the optimal policy. Owing to the algorithmic advancement of recent deep RLs, we propose to circumvent the unobservable true label issue by maximizing the reward related to the learning signals in the model.

In this study, we propose a novel framework combining neural networks with RL strategies. Our method selects ROIs containing temporally meaningful information about each ROI signal and explores the functional relations of the selected ROI sets for each subject considering individual variability. Compared with other feature selection methods widely used in fMRI analysis, the RL algorithm allows the selection of ROIs automatically and individually. Because the different ROI sets may have an impact on the resulting functional relations (Sohn et al., 2015), the RL-based selected ROI sets can help avoid the learning of functional relations between less important ROIs, as well as capture complex and subtle functional changes caused by eMCI more robustly.

To represent functional relations, we used a graph convolution network (GCN) (Kipf and Welling, 2016). Graph-theory-based methods have been previously adopted for fMRI (Medaglia, 2017; Wang et al., 2010), as it contributes to its ability to model topological properties intrinsic to brain networks. The brain, a complex network system, can be represented by a set of nodes and edges, where the regions of voxels can be defined as vertices, i.e., vertex features, and their functional or structural connections can be regarded as edges. One of the graph-based methods in neuroimaging studies, GCN which is a generalization of a CNN for a non-Euclidean domain, has received attention as a potential tool for discriminating between groups or individuals in network-level brain systems (Ktena et al., 2018; Parisot et al., 2018; Yan et al., 2019). Similar to conventional methods that use FC to capture functional information between regions, a GCN can capture local and global nonlinear patterns of a topological organization.

To summarize, our model constructs ROI sets having class-discriminative and informative characteristics for each subject. Then, it represents their functional relational properties for clinical utilization. Our contributions can be summarized as follows: we propose a novel framework for automatic region selection and modeling the regions' functional relation. We analyze the ROIs selected from our proposed method and compare them with the MCI relevant regions reported in neuroscience studies. Based on the results, we report eMCI-related information and individual differences. We, finally, validate the effectiveness of our proposed method using the ADNI public dataset by comparing its performance to those of other methods.

2. Materials and preprocessing

2.1. ADNI cohort

We used data from 101 subjects from the ADNI cohort (in ADNI2 and ADNI GO). Specifically, we collected a dataset comprising 53 individuals with eMCI (33F/20M) and 48 cognitively normal (CN; 27F/21M) individuals. Their mean ages were 75.2 ± 6.2 and 71.7 ± 7.1, respectively. From the longitudinal data, we obtained total 316 samples (136 CN and
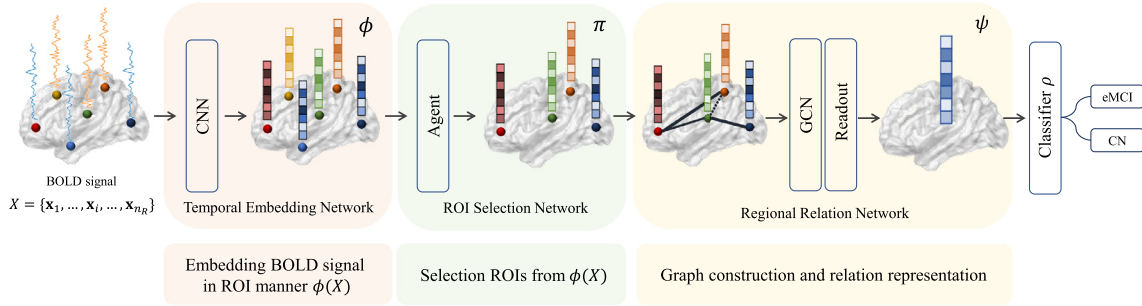
Fig. 1. Overview of our proposed framework for eMCI classification. The temporal embedding network ϕ transforms the input BOLD signal. From the embedded features of each ROI involving meaningful information in BOLD, the agent π selects ROIs. Subsequently, the graph comprising the selected ROIs is fed into a GCN to represent regional relations. Finally, the learned graph features are used in the classifier ρ. (n_R: number of ROIs; CNN: convolution neural network; GCN: graph convolution network).

180 eMCI). The images were scanned using 3.0T Philips Achieva scanners in multi-center with following protocol and parameters: Repetition Time (TR) = 3000ms, Echo Time (TE) = 30ms, flip angle = 80°, acquisition image size = 64 × 64, 48 slices, 140 time points, and a voxel thickness = 3.3mm.

2.2. Preprocessing

In this work, the dataset was preprocessed using the Data Processing Assistant for Resting-State fMRI (Yan et al., 2016) based on SPM12[4] and REST[5]. During preprocessing, we discarded the first 10 time-points for each subject for magnetization equilibrium. The remaining volumes were then spatially normalized to the MNI space and resliced to a voxel size of $2 \times 2 \times 2$mm^3. Then, the images were smoothed by 4mm full width at half maximum (FWHM) using a Gaussian kernel to reduce spatial noise. We band-pass-filtered the temporal BOLD signals from 0.01 to 0.1 Hz to obtain low-frequency fluctuations in rs-fMRI. For regional mean time signals, we divided the brains spatial domain into 114 ROIs based on the 17 networks from the functional atlas of Thomas Yeo et al. (2011), and then took the average of voxels within in each ROI for each subject. The whole preprocessing above resulted in BOLD signals $X \in \mathbb{R}^{n_R \times n_T}$, where n_R and n_T denote the number of ROIs ($n_R = 114$) and volumes ($n_T = 130$), respectively.

3. Proposed methods

In this section, we describe our novel neural-network-based framework for eMCI classification, as schematized in Fig. 1. We introduce our framework by defining it as a set-input neural network (Zaheer et al., 2017), based on our hypothesis that each subject has a different ROI set composed of ROI elements that are functionally meaningful for disease identification. Our proposed framework comprises a permutation-equivariant network and a permutation-invariant network, thereby satisfying the permutation-invariant condition that should be met for a set-input neural network. Although general DL models cannot handle fixed-length variables across samples for different sizes of sets across subjects, a set-input neural network can do so effectively. In addition, it can successfully capture patterns of input instances such as ROI signals, and represent subtle abnormalities in the input instances.

Given the preprocessed rs-fMRI signals of the n-th sample, $n = 1, \ldots, n_s$, where n_s is the number of training samples, and $X^n = \{\mathbf{x}_1^n, \ldots, \mathbf{x}_i^n, \ldots, \mathbf{x}_{n_R}^n\} \in \mathbb{R}^{n_R \times n_T}$ with its elements $\mathbf{x}_i^n \in \mathbb{R}^{1 \times n_T}$ as the ith ROI signal, the signals first pass through a region-wise or ROI-wise, CNN-based temporal embedding network ϕ (Section 3.1) for the extraction of meaningful information which includes temporal fluctua-

tions and functional dynamics. Subsequently, an ROI selection network, π, (Section 3.2) selects *significant* ROIs out of all the input ROIs. Using a graph-based regional relation network ψ (Section 3.3), we model the functional relations among the selected ROIs at the individual level while simultaneously enhancing the diagnosis power at the group level. Hereafter, we omit sample index n for simplicity. It should be noted that all these modules in our framework are trained using two types of learning schemes, supervised learning and RL, in an end-to-end manner. The three modules of our framework, the temporal embedding network (Section 3.1), ROI selection network (Section 3.2), and regional relation network (Section 3.3), as well as their learning schemes (Section 3.4) are described in detail as follows.

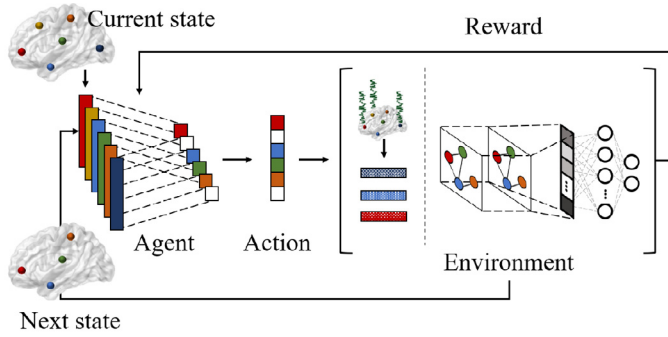### 3.1. Temporal embedding network

We first embed rs-fMRI data in an ROI-wise manner using a CNN, which is a special form of deep neural network and one of the most widely used networks in the field of neuroimaging (Hosseini-Asl et al., 2016; Shen et al., 2017). It is mainly composed of a convolution kernel and an activation function, and optionally, a pooling operation (Shen et al., 2017). The convolution kernel learns the local features of the input by sharing the filter weight and moving the filter both vertically and horizontally. Typically, convolutional layers are stacked as an effective class-relevant feature extractor during image analysis (Gu et al., 2018). These features are followed by an activation function operation for nonlinearity, beneficial for learning complex fMRI data in neural networks. We omit the pooling operation that summarizes features to preserve the fine-grained information inherent in fMRI data. Finally, the activated features are fed into the next module in the framework.

Specifically, we use a one-dimensional kernel convolution operation (1D convolution) on the temporal axis; it is therefore regarded as a temporal CNN. By performing convolution of time-series data, we can extract the temporal features of the BOLD signals. Furthermore, consecutive convolution operations involve the application and sliding of a temporal filter over the signal data, such that the dynamics properties of the original BOLD signals are retained in the output, $\phi(\mathbf{x}_i), \forall i = 1, \ldots, n_R$. To learn the inherent temporal patterns of ROIs in common, a 1D convolution filter is shared across the ROI signals, so, $\phi(X) = \{\phi(\mathbf{x}_1), \ldots, \phi(\mathbf{x}_i), \ldots, \phi(\mathbf{x}_{n_R})\}$.

In addition, the use of 1D convolution ensures that our network satisfies the permutation-equivariant condition of a deep set-input neural network. Because the convolution operates in an ROI-independent manner, our temporal embedding network can be used as a permutation-equivariant network. More precisely, for a given rs-fMRI image X, the network extracts the temporal features of the BOLD signal of each ROI, $\phi(\mathbf{x}_i) \in \mathbb{R}^{n_T' \times n_F}$ where n_T' and n_F denote the dimensions of convolved timepoints and feature maps, respectively. In the training phase, n_F

---

[4] https://www.fil.ion.ucl.ac.uk/spm/

[5] https://www.nitrc.org/projects/rest/

Fig. 2. Formulation of an interaction between the agent and the environment. The agent selects ROIs that have useful and class-discriminative information for disease identification. The environment shows the state, i.e., the embedded features, to the agent. Based on the given current state, the agent makes an action of selecting ROIs. For this result, the agent receives the corresponding reward from the environment. The current action affects the environment and the next state. The agent is trained such that the rewards from the environment are maximized by repeating these steps.

is controlled as a hyper-parameter and can be regarded as a multi-perspective feature of the temporal pattern. Hereafter, the final output, i.e., all the ROIs of temporally embedded features, is considered as a set.

3.2. ROI selection network

Owing to the individual variability in the functional characteristics of human brains, which can be affected by brain diseases or disorders, we hypothesize that different ROIs for each subject may be informative or useful for identifying disease-identifiable functional patterns. Inter-subject variability shows that group properties are not precisely representative of individuals. Based on this assumption, we introduce an ROI selection network π to filter the ROIs to facilitate disease-identifiable functional feature representation in the ensuing module. The network π ensures that all ROIs from the embedded BOLD signal are divided into two subsets. One is the set with class-discriminative information and the other is the set without this information. However, it is problematic for this network to use well-known *supervised learning* strategies that exploit paired data and labels directly. No clear criterion exists regarding which ROIs are diagnostically discriminative for a subject. In other words, no ground truth for disease-discriminative ROIs are available to train the network.

To model a selection network, hereafter referred to an agent, that can automatically find the disease-discriminative ROI subset without any ground truth or prior knowledge, we formulate the RL framework, which we then use to construct the ROI selection network. We regard our ROI selection problem as a Markov decision process (MDP (Sutton and Barto, 2018)). We formalize the MDP as a tuple $\mathcal{M} := \langle S, A, P, r, \gamma \rangle$, where S, A, P, r, and γ denote a set of states, a set of actions, a state transition matrix, a reward signal, and a *discounted factor*, respectively (Sutton and Barto, 2018). For a clearer depiction of our formulation, the entire interaction between the environment and the agent is illustrated in Fig. 2.

Generally, RL frameworks are categorized into *model-based* and *model-free* algorithms (Sutton and Barto, 2018). In model-free RLs, it is not necessary to model the environment. The agent can instead learn an *optimal* policy directly. Because there are no particular factors interrupting ROI selection using rs-fMRI, we focus on model-free RL. Furthermore, among the model-free frameworks, we use a policy-based method in which the policy can be parameterized (Sutton and Barto, 2018). A significant advantage of parameterizing policy according to the probabilities in action preferences is that it can achieve an optimal stochastic approach with imperfect information (Sutton and Barto, 2018). Thus, we use a policy-based RL algorithm.

Before describing our network, we design a training process for the ROI selection network π, or the agent. In our case, the environment provides state s, i.e., the feature representation from the set of ROIs via the embedding network ϕ, and the reward r according to the agent's action a. To train our ROI selection network, we use the REINFORCE algorithm (Sutton et al., 2000). Our framework first generates an episode $(s_0, a_0, r_1, ..., s_{T-1}, a_{T-1}, r_T)$, where T is the episode length. The initial state s_0 is denoted by $s_0 = \phi(X; \theta_\phi^{(0)}) = \{\phi(\mathbf{x}_i; \theta_\phi^{(0)}) | i = 1, ..., n_R\}$, where

$\theta_\phi^{(0)}$ denotes the parameter of the temporal embedding network ϕ at the 0th iteration (i.e., the initial setting). Then, our ROI selection network π decides an action $\pi(s_0; \theta_\pi^{(0)}) = a_0 \in \{0, 1\}^{n_R}$, where '1' and '0' denote the ROI selection and non-selection, respectively. Now, the bth state in the bth iteration can be generalized as follows:

$$s_b = \left\{ \phi\left(\mathbf{x}_i; \theta_\phi^{(b)}\right) \Big| a_{b-1,i} = 1, i = 1, ..., n_R \right\} \tag{1}$$

where the $(b-1)$th action for the ith element is estimated as follows:

$$a_{b-1,i} = \pi\left(s_{b-1}; \theta_\pi\right) \in \{0, 1\}. \tag{2}$$

Finally, the classification loss at the bth iteration, detailed in Eq. (11) is used as the bth reward signal for the given action.

Because we want to train our policy network to maximize the total reward over the entire process in an episode, we consider a so-called *delayed reward* (Sutton and Barto, 2018) at each time point a decision is made. Therefore, we use a discount factor, $\gamma \in [0, 1]$, as a hyperparameter, to control the effect of the delayed reward. When γ is close to one, the agent seeks future-oriented rewards; when it is close to zero, it means the agent weighs the reward of the present situation higher. The future values of the rewards decay exponentially according to γ. The delayed reward affects ROI selection considering not only the immediate reward of the ROI subset selected from the current state, but also the future reward of the ROI subset from the next state. With the given reward r_t and discount factor γ, we define the total return G_t as follows:

$$G_t = \sum_{l=t+1}^{T} \gamma^{l-t-1} r_l. \tag{3}$$

Finally, we update the tunable parameter of the agent to optimize the sequential actions by performing a gradient ascent to maximize the expected total return $\mathbb{E}[G_t]$. To do so, we estimate the tth gradient as follows:

$$\Delta\theta_\pi = \alpha G_t \nabla \ln \pi(s_t; \theta_\pi) \tag{4}$$

where α is the learning rate.

In this study, we use an ROI-wise CNN for the ROI selection network π. The temporal embedding network first learns meaningful features and emphasizes on them in an ROI-independent manner. Then, our ROI selection network π selects a subset of ROIs containing meaningful informative features using an interactive trial-and-error learning strategy.

3.3. Regional relation network

To build a regional relation network ψ for the selected ROIs, we use the GCN (Kipf and Welling, 2016) considering the following advantages: graph representation learning and permutation invariance. One of our contributions is that our framework is devised to manage individual variability in rs-fMRI. Similar to the ROI selection network, the network for regional relation representation learning has no limitation on the input size. Unlike most deep models, which require fixed input variables and cannot easily cope with varying input sizes, GCN is practical in the sense that it can overcome this constraint. Owing to the

unordered attributes of graph nodes, each subject and its corresponding nodes are regarded as set and set elements, respectively. In addition, it is not necessary to have graphs of the same size. Therefore, GCN satisfies the permutation-invariant condition.

3.3.1. Graph construction

To capture the relationship between selected regions, we construct a graph. The input graph is defined as a weighted graph $\mathcal{G} = \{\mathcal{V}, \mathcal{E}, \mathcal{W}\}$, where $\mathcal{V}$ is a set of nodes and $\mathcal{E}$ is a set of edges. $\mathcal{W}$ denotes the weight of the adjacency matrix of the weighted connection between the edges. $z_i \in Z$ is an attribute of the ith node, where Z is the general form of the matrix of the node attributes. In our study, the node attributes Z (i.e., features) are defined as selected ROIs of each subject from the ROI selection network as follows:

$$Z = \text{concat}\left(\left\{\phi\left(\mathbf{x}_i; \theta_\phi^{(b)}\right)\middle| a_{b-1,i} = 1, i = 1, \ldots, n_R\right\}\right) \in \mathbb{R}^{n'_R \times n_F} \quad (5)$$

where concat is the concatenation operator. From Eq. (5), Z becomes a matrix comprising of only the selected ROIs, enhancing the classification accuracy. To perform graph convolution, the edges should present relational information between paired nodes. We construct an undirected weighted graph to adjust the importance between ROIs such that the edge $e_{ij} = e_{ji} \in \mathcal{E}$ or the weighted adjacency matrix $\mathcal{W}_{ij}$ represents a similarity between a feature vector $\mathbf{z}_i$ of the ith node and a feature vector $\mathbf{z}_j$ of the jth node, defined as follows:

$$\mathcal{W}_{ij} = \exp\left(-\frac{\text{sim}(\mathbf{z}_i, \mathbf{z}_j)}{2\sigma^2}\right) \quad (6)$$

where $\text{sim}(\cdot, \cdot)$ is the similarity operation, and σ is the predefined kernel width. Eq. (6) implies that if the inputs have similar embedding values; this indicates a high similarity between the corresponding ROIs. Note that when different ROIs are selected for each subject, graph $\mathcal{G}$ from the selection network also differs for each subject.

3.3.2. Graph convolution networks

The main building block in our regional relation network ψ leverages spectral graph convolution based on a graph Fourier transform (GFT) (Chung and Graham, 1997). From the weighted graph with selected ROIs, defined in Section 3.3.1, spectral graph convolution is performed by first computing the eigendecomposition of the graph Laplacian $L = D - \mathcal{W}$, followed by a GFT, where $D = \sum_j \mathcal{W}_{ij} \in \mathbb{R}^{n'_R \times n'_R}$ is the diagonal degree matrix in the graph, and n'_R denotes the number of selected ROIs. Specifically, the normalized form of the graph Laplacian $L = I - D^{-1/2}\mathcal{W}D^{-1/2}$, where $I \in \mathbb{R}^{n'_R \times n'_R}$ is an identity matrix, is decomposed as $L = U\Lambda U^\top$ by its eigenvectors $U \in \mathbb{R}^{n'_R \times n'_R}$ and the corresponding diagonal matrix of the eigenvalues $\Lambda \in \mathbb{R}^{n'_R \times n'_R}$.

Given a filter g_θ that is a diagonal matrix parameterized with Fourier coefficients $\theta \in (\mathbb{R})^{n'_R}$, the spectral convolutions of the signal $\mathbf{z} \in \mathbb{R}^{n'_R}$ (assuming a single scalar feature per node) are defined as $g_\theta * \mathbf{z} = g_\theta(L)\mathbf{z} = g_\theta(U\Lambda U^\top)\mathbf{z} = U g_\theta(\Lambda)U^\top \mathbf{z}$ with properties of GFTs. Here, with regard to filter approximation, we use Kth order Chebyshev polynomial filters (Defferrard et al., 2016), $g_\theta(L)\mathbf{z} = \sum_{k=0}^K \theta_k T_k(\tilde{L})\mathbf{z}$, which provides the benefits of K-localization and cost-effective computation of convolution. $\tilde{L} = \frac{2}{\lambda_{max}}L - I$ is the scaled Laplacian matrix and λ_{max} is the maximum eigenvalue Λ. θ_k is a coefficient of the Chebyshev polynomial.

In Kipf and Welling (2016), the author proposed a simplified GNN of Defferrard et al. (2016) as $K = 1$ of the Chebyshev polynomial and $\lambda_{max} = 2$, as follows:

$$f_\theta \star \mathbf{z} \approx \theta\left(I + D^{-\frac{1}{2}}\mathcal{W}D^{-\frac{1}{2}}\right)\mathbf{z} \quad (7)$$

where θ is a single parameter that prevents overfitting by constraining the number of parameters in the polynomial. Furthermore, they introduced renormalization trick $I + D^{-\frac{1}{2}}\mathcal{W}D^{-\frac{1}{2}}$ to $\tilde{D}^{-\frac{1}{2}}\tilde{\mathcal{W}}\tilde{D}^{-\frac{1}{2}}$, where

$\tilde{\mathcal{W}} = \mathcal{W} + I$ and $\tilde{D} = \sum_j \tilde{\mathcal{W}}_{ij}$ are the adjacency matrix and degree matrix from the renormalization trick, respectively. Finally, our regional relation network ψ based on graph convolution for the general form of node features Z is defined as follows:

$$\psi(Z) = \tilde{D}^{-\frac{1}{2}}\tilde{\mathcal{W}}\tilde{D}^{-\frac{1}{2}}Z\theta \quad (8)$$

where $\theta \in \mathbb{R}^{n_F \times n_H}$ is a trainable parameter, i.e., the weight for linear mapping of the feature (input or hidden features), and n_H denotes the size of the hidden features of the GCN.

The key idea behind the regional relation network ψ is that the vertex features are learned by reflecting and accommodating features of the neighboring vertices. The node features in our framework are defined for the selected ROIs from the embedding and ROI selection networks, and the weighted edges represent the similarities between these pairs. The functional relations among the selected ROIs in a high-dimensional space are represented by training our GCN.

3.3.3. Readout layer and classifier

For graph classification, it is necessary to represent node features in a fixed-length form while maintaining meaningful information about the graph. Xu et al. (2018) defined a graph as a multiset that has repeating elements and they investigated various pooling methods for graphs. Among these methods, summation pooling was able to capture entire node features, and max pooling was found capable of capturing representative elements of the entire graph. Inspired by their study, we use the readout function (Cangea et al., 2018) defined from the hidden representations of nodes to summarize the entire graph as a fixed representation. Concisely, we define the readout function for a hidden feature H from a regional relation network as follows:

$$\mathbf{f} = \text{ReadOut}(H) = \text{concat}\left(\sum_{i=1}^{n'_R} \mathbf{h}_i, \max_{j=1}^{n'_R} \mathbf{h}_j\right) \in \mathbb{R}^{2n'_H} \quad (9)$$

where $\mathbf{h}_i \in H$ is the hidden feature vector from the regional relation network of the ith node, and n'_H is the output dimension of the feature. We use node-wise summation pooling to capture all the node features of the ROIs in the graph. Additionally, we use max-pooling in a node-wise manner to improve the discriminative power of the diagnosis. Using the readout function, the final output decision label for each subject can be estimated using $\hat{\mathbf{y}} = \rho(\mathbf{f})$ where ρ denotes the feed-forward neural network for classification.

3.4. Optimization

To optimize the temporal embedding network ϕ, ROI selection network π, regional relation network ψ, and classifier ρ jointly in an end-to-end manner, we leverage two types of learning schemes, namely, supervised learning and RL. For supervised learning, a widely used binary-cross-entropy-loss method is used for the three networks: temporal embedding ϕ, regional relation representation ψ, and classification ρ. To be specific, the tunable parameters of ϕ, ψ, and ρ, denoted as θ_ϕ, θ_ψ, and θ_ρ, are optimized as follows:

$$\theta_\phi^*, \theta_\psi^*, \theta_\rho^* = \arg\min_{\theta_\phi, \theta_\psi, \theta_\rho} \text{BCE}\left(\hat{\mathbf{y}}, \mathbf{y}; \theta_\phi, \theta_\pi, \theta_\psi, \theta_\rho\right) \quad (10)$$

where $\hat{\mathbf{y}}$ and $\mathbf{y}$ denote the predicted and the ground-truth labels, respectively. Meanwhile, for the ROI selection network π, we use the REINFORCE algorithm (Sutton et al., 2000). Specifically, the trainable parameters θ_π of selection network π are guided by reward r_b at the bth step, defined as follows:

$$r_b = -\text{BCE}\left(\hat{\mathbf{y}}, \mathbf{y}; \theta_\phi^{(b)}, \theta_\pi^{(b)}, \theta_\psi^{(b)}, \theta_\rho^{(b)}\right), \quad (11)$$

and optimized to maximize the accumulated total rewards over T steps in an episode:

$$\theta_\pi^* = \arg\max_{\theta_\pi} \sum_{b=1}^T \gamma^b r_b. \quad (12)$$

In Eq. (12), because the reward for the agent is defined with the negative loss based on both the regional relation network and the classifier, we believe that the agent infers the informativeness of the ROIs, based on the temporally embedded features, in the ensuing regional relation network and classifier indirectly. In other words, the agent observes temporally embedded features of each ROI and performs selection individually but it is also capable of inferring each region's importance for regional relation representation for classification.

The pseudo-algorithm to train our proposed model is presented in Algorithm 1 .

Algorithm 1: Pseudo-algorithm to train the parameters of our proposed model

Input: Training dataset $\{X^{(n)}, \mathbf{y}^{(n)}|n = 1, ..., n_s\}$; network architectures θ_ϕ, θ_π, θ_ψ, and θ_ρ; # of pre-training n_p; # of mini-batches n_B, a mini-batch size M and a discounted factor γ; a stochastic gradient descent optimizer SGD and its hyperparmeters set $\boldsymbol{\eta}$

Output: Optimized network parameters, θ_ϕ^*, θ_π^*, θ_ψ^* and θ_ρ^*

```
// Pre-training of temporal embedding, regional
   relation, and classification networks
```
1 **for** $i = 1, ..., n_p$ **do**
2 　**for** $k = 1, ..., n_B$ **do**
3 　　Draw a mini-batch set $\{X^{(m)}, \mathbf{y}^{(m)}|m = 1, ..., M\}$
4 　　$\mathbf{f}^{(m)} \leftarrow \text{ReadOut}(\psi(\phi(X^{(m)}; \theta_\phi); \theta_\psi))$
5 　　$\hat{\mathbf{y}}^{(m)} \leftarrow \rho(\mathbf{f}^{(m)}; \theta_\rho)$
6 　　$\mathcal{L}^{(m)} \leftarrow \text{BCE}(\hat{\mathbf{y}}^{(m)}, \mathbf{y}^{(m)})$
7 　　$\theta_\phi, \theta_\psi, \theta_\rho \leftarrow \text{SGD}(\frac{1}{M}\sum_{m=1}^{M}\mathcal{L}^{(m)}; \theta_\phi, \theta_\psi, \theta_\rho, \boldsymbol{\eta})$

```
// Joint training of temporal embedding, ROI selection,
   regional relation, and classification networks
```
8 **while** *not converged* **do**
9 　**for** $k = 1, ..., n_B$ **do**
10 　　Draw a mini-batch set $\{X^{(m)}, \mathbf{y}^{(m)}|m = 1, ..., M\}$
11 　　$\phi(X^{(m)}) \leftarrow \{\phi(\mathbf{x}_i^{(m)})|i = 1, ..., n_R\}$
12 　　Generate episodes $(s_0^{(m)}, a_0^{(m)}, r_1^{(m)}, ..., s_{T-1}^{(m)}, a_{T-1}^{(m)}, r_T^{(m)})$ by recursively applying π and Eq. (11)
13 　　**for** $t = 0, 1, ..., T - 1$ **do**
14 　　　$G_t^{(m)} \leftarrow \sum_{l=t+1}^{T} \gamma^{l-t-1} r_l^{(m)}$
15 　　　$\mathcal{L}_t^{(m)} \leftarrow G_t^{(m)} \ln \pi(s_t^{(m)}; \theta_\pi)$
16 　　　$\theta_\pi \leftarrow \text{SGD}(-\frac{1}{M}\sum_{m=1}^{M}\mathcal{L}_t^{(m)}; \theta_\pi, \boldsymbol{\eta})$
17 　　Get $Z^{(m)}$ using $\phi(X^{(m)})$ and $a_{T-1}^{(m)}$ by Eq. (5)
18 　　$\mathbf{f}^{(m)} \leftarrow \text{ReadOut}(\psi(Z^{(m)}; \theta_\psi))$
19 　　$\hat{\mathbf{y}}^{(m)} \leftarrow \rho(\mathbf{f}^{(m)}; \theta_\rho)$
20 　　$\mathcal{L}^{(m)} \leftarrow \text{BCE}(\hat{\mathbf{y}}^{(m)}, \mathbf{y}^{(m)})$
21 　　$\theta_\phi, \theta_\psi, \theta_\rho \leftarrow \text{SGD}(\frac{1}{M}\sum_{m=1}^{M}\mathcal{L}^{(m)}; \theta_\phi, \theta_\psi, \theta_\rho, \boldsymbol{\eta})$

---

4. Experiments

4.1. Experimental setting

In our experiment, we used three convolution layers to filter the rs-fMRI signal in the temporal filtering network ϕ. The kernel size of the first convolution layer is 65 with five output filter maps. The kernel size of the second layer was 30 with 10 output filter maps. In the last layer, we used a CNN for global temporal embedding with a kernel size of 37 and filter map size of 20. The ROI selection network π had a kernel size of 20 with one output filter map. Therefore, the dimensions of the output of the agent, i.e., the input of the regional relation network, was $\mathbb{R}^{n_R' \times 20}$, where n_R' is the number of selected ROIs. In addition, we used two graph convolution layers for the regional relation network ψ, with

a hidden feature size of 10 in the first layer and hidden dimension 5 in the second layer. Then, the output dimension of the readout function was $\mathbb{R}^{10}$, due to the concatenation of the summed and maximum values in each dimension by Eq. (9). Finally, a fully connected single layer was used as the classifier ρ. For pretraining, we set n_p as 10. The activation function for nonlinearity in all the convolution layers was an exponential linear unit (eLU) function, and the softmax function was used in the final fully connected layer. In Eq. (6) of the graph construction, we used the correlation distance between the nodes i.e., ROIs, as follows:

$$\text{sim}(\mathbf{z}_i, \mathbf{z}_j) = 1 - \frac{(\mathbf{z}_i - \bar{\mathbf{z}}_i)^\top (\mathbf{z}_j - \bar{\mathbf{z}}_j)}{\left\|\mathbf{z}_i - \bar{\mathbf{z}}_i\right\|_2 \left\|\mathbf{z}_j - \bar{\mathbf{z}}_j\right\|_2} \tag{13}$$

where $\bar{\mathbf{z}}_{i/j}$ denotes a vector with the elements set by the mean of $\mathbf{z}_{i/j}$. Notably, σ in Eq. (6) represents the mean value of the correlation distance between the nodes, based on Parisot et al. (2018). To avoid overfitting, we used layer normalization in all the convolution layers, Gaussian dropout in the final fully connected layer, and an elastic net regularizer with $l_1 = 0.005$ and $l_2 = 0.005$. Moreover, a label-smoothing method (Szegedy et al., 2016) was used for the fully connected layer. The epoch and minibatch sizes were 50 and 5, respectively. A Nadam optimizer (Dozat, 2016) was used for training, with a learning rate of 0.001. We implemented our model using TensorFlow.[6]

4.2. Comparative Methods

To validate our proposed method, we considered multiple comparative conventional machine learning algorithms and recent deep neural networks. Specifically, we employed the following comparative models:

- FC-SVM: We trained a support vector machine (SVM) with FC computed using Pearson correlation. As the input, the FC matrix was flattened to a vector form using an upper triangle. The input dimensions were $(114 \times 113)/2 = 6, 441$. For training, we used a linear SVM and considered a slack variable C in $\{10^{-5}, ..., 5\}$. A grid search strategy was used to select the optimal model.

- CNN: A conventional CNN was used based on the same kernel and feature map size as that of our temporal embedding network in the BOLD input. After performing temporal embedding, the features were fed into a spatial convolution layer that was added in the ROI axis (114,1). Those features with a densely connected layer were used for classification.

- SA-CNN: This is self-attention (Vaswani et al., 2017) mechanism with a conventional CNN. We specifically utilized our temporal embedding network to extract the temporal features. Then, we estimated an attention mask using the self-attention framework (Vaswani et al., 2017). The attention mask was Hadamard produced to the represented features. Finally, we used a spatial convolution layer for spatial feature extraction and a densely connected layer to linearly map the features to the output dimension.

- LSTM-DG (Dvornek et al., 2019): We trained the original network structure reported in Dvornek et al. (2019) based on a long short-term memory network for discriminative and generative tasks. Specifically, we used 50 and 20 hidden units in the first and second layers, respectively. In the final layer, a dense connection was used for the classification. The sliding window method was used as the input, with a predefined window size of 30 and a stride of 1 in the BOLD signal.

- BrainNetCNN (Kawahara et al., 2017): To train the FC, we used the BrainNetCNN based on *edge-to-edge, edge-to-node*, and *node-to-graph* layers. We implemented the network using two edge-to-edge layers with 10 output feature maps, one edge-to-node layer with 20 output feature maps, and one node-to-graph layer with 40 output feature maps, to train over a limited number of training samples efficiently.

Table 1
Demographics of ADNI subjects. MMSE: mini-mental state examination score; CDR: clinical dementia rating.

	CN	eMCI
Number of subjects	48	53
Sex (Female/Male)	27/21	33/20
Age (Mean ± SD)	71.2 ± 6.2	71.7 ± 7.1
Education (Mean ± SD)	16.33 ± 2.33	15.82 ± 2.93
Race		
Asian	0	2
Black	2	0
White	40	44
More than one	1	2
Unknown	5	5
MMSE	28.84 ± 1.42	28.25 ± 1.67
CDR	0.06 ± 0.18	0.48 ± 0.23

- GNN (Parisot et al., 2018): We employed a GNN with features selected via linear regression utilizing elastic net regularization (Zou and Hastie, 2005)[7]. By defining a node as a subject; thus, a population graph was constructed. We set the K order of the Chebyshev polynomial as 3 in the GNN and used two GNN layers. In our experiments, the phenotypes considered for the edge weight were sex and age.
- GAPool (Knyazev et al., 2019): Our RL-based ROI selection network can be understood as a type of pooling operation in the ROI dimension. In this sense, we also compared the pooling method in a graph neural network (Knyazev et al., 2019). The attention threshold value was empirically set to 0.3. To build the model, we used a conventional GCN with two layers (Kipf and Welling, 2016).
- Ours (Bandit): To test the effectiveness of RL, we trained the network without a delayed reward. Thus, we generated an episode of $T = 1$ and set our method as a multi-armed bandit problem. From this setting, the agent worked as a simple gating mechanism for ROI selection trained by supervised learning.

To evaluate the performance of the competing methods, we conducted a 10-fold cross-validation. Specifically, we split the data into 10 parts and used eight folds as training data, one fold as validation data, and another one fold as test data. It should be noted that because we considered an eMCI identification with a cross-sectional sample, the dataset partition was performed in a subject-based manner. In other words, we divided the 101 subjects into 10 folds; thus, samples of the same subject were assigned to the same fold. This guaranteed that none of the competing methods, including our proposed method, take advantage of the information of the samples from the same subjects during testing. Furthermore, we repeated this process 10 times to measure the effectiveness of the proposed method and reported the averaged performance with standard deviation. For a quantitative measurement, we calculated the following four metrics: accuracy (ACC = TP + TN/(TP + TN + FP + FN)), sensitivity (SEN = TP/(TP + FN)), specificity (SPEC = TN/(TN + FP)), and area under the receiver operating curve (AUC), where TP, TN, FN, and FP denote true positive, true negative, false positive, and false negative, respectively.

4.3. Performance comparison

Table 2 summarizes the diagnostic results. Specifically, our proposed method achieved the best accuracy (74.42 ± 1.80) and AUC (0.7438 ± 0.0161) with large margins compared to the other methods. Compared with BrainNetCNN (Kawahara et al., 2017), which used the entire brain relation represented by FC, our network used only the selected ROIs and their relation representation for clinical decision making. Furthermore,

while our method individually selected ROIs, GNN (Parisot et al., 2018) used the region-related features via sparse representation learning in a group-wise manner. Using the selected ROIs' features in an individual manner, our approach showed desirable performance, in addition to balanced sensitivity and specificity. Compared with GAPool (Knyazev et al., 2019), our model exploited a policy network trained in RL to reduce the size of the graph via an effective selection of nodes, i.e., the ROIs, as a counterpart of the pooling strategy. From the trial-and-error strategy used in RL, our proposed method learned the optimal actions, which further enhanced its performance. Therefore, our method achieved a good performance in all the metrics. Additionally, compared with the Bandit setting, our network achieved superior performance, with regard to the ACC and AUC. The delayed reward mechanism was also found to improve the performance of our network. We also conducted a Wilcoxon signed-rank test to validate the effectiveness of our proposed method and found that it demonstrated statistical significance as compared with the other methods, with p-values of 0.01 and 0.01 for the ACC and AUC, respectively.

5. Discussion

5.1. Ablation Studies

In this section, we investigate the effects of each regional relation network (GCN), and the ROI selection network (agent). Because our framework is composed of two components, agent π and GCN ψ, we experimented to determine which factor has the greatest impact on performance. These experiments can be categorized as follows:

- ϕ (Ours w/o Agent and GCN) : To verify the effects of agent π and GCN ψ, we trained only the temporal embedding network. We used the same kernel size, number of feature maps, and number of layers as those used in our temporal embedding network. For classification, we modified the structure of the last layer to the sum pooling and dense connection layers.
- $\phi + \psi$ (Ours w/o Agent) : We investigated the efficacy of our ROI selection network π by eliminating it from the framework. The entire framework was constructed using only the temporal embedding and regional relation networks. Therefore, no ROIs were selected. All the ROIs were fed into the network; thus, the last layer for classification was changed by the Readout function of the graph of the entire ROI.
- $\phi + \pi$ (Ours w/o GCN) : We removed our GCN ψ to observe changes in performance. To confirm the effect of the regional relation network, we used sum pooling after the agent. In this setting, the reward of the agent was defined using the sum relation loss instead of the loss involved in the graph-based relation.

The results of the average performance with standard deviations are shown in Fig. 3. Based on the results, we conclude the following: the proposed method combining an agent and GCN demonstrated the best performance compared to the other settings. From 'Ours w/o Agent,' it can be concluded that the use of an agent significantly improved the performance across all settings. Because the agent selected ROIs, which possibly involved informative characteristics for disease identification, it had a positive effect on enhancing performance by removing distracting features (i.e., class-irrelevant features). Observing the performance degradation in 'Ours w/o GCN,' we could understand the importance of using regional relations for eMCI identification.

5.2. Analyses of agent and GCN

In our framework, the agent selected ROIs that were determined as meaningful information from the current state or the temporally embedded features. To determine how the selected ROIs and non-selected ROIs are distributed, we visualized all the features of the ROIs from the temporal embedding network. With randomly selected models among the 10 folds, the features were projected onto a two-dimensional (2D) space

---

[7] We empirically selected the elastic net regularization (Zou and Hastie, 2005) to select features, rather than the recursive feature elimination originally proposed in Parisot et al. (2018).

Table 2

A performance comparison of comparative methods on ADNI dataset. Boldface indicates the highest value in each metric. ⋆ denotes the statistical significance in $p < 0.01$. Our proposed method (Ours) is shown significantly improved results compared to other methods.

Methods	AUC	ACC (%)	SEN (%)	SPEC (%)
SVM	$0.5429 \pm 0.1399\star$	$56.93 \pm 14.48\star$	63.86 ± 14.64	44.68 ± 23.24
CNN	$0.5695 \pm 0.0159\star$	$57.71 \pm 2.05\star$	68.49 ± 6.01	45.42 ± 5.89
SA-CNN	$0.5752 \pm 0.0574\star$	$60.41 \pm 7.05\star$	$\mathbf{79.97 \pm 16.70}$	35.17 ± 20.88
LSTM-DG	$0.6425 \pm 0.0185\star$	$63.50 \pm 1.90\star$	62.76 ± 3.10	65.73 ± 1.22
BrainNetCNN	$0.6723 \pm 0.0201\star$	$67.62 \pm 2.02\star$	67.21 ± 5.00	67.08 ± 5.98
GNN	$0.5900 \pm 0.0104\star$	$59.37 \pm 0.80\star$	52.03 ± 4.66	64.79 ± 3.48
GAPool	$0.5064 \pm 0.0317\star$	$51.48 \pm 3.95\star$	58.31 ± 15.62	43.08 ± 13.95
Ours (Bandit)	0.7295 ± 0.0143	73.07 ± 1.39	70.88 ± 3.01	$\mathbf{75.03 \pm 2.86}$
Ours	$\mathbf{0.7438 \pm 0.0161}$	$\mathbf{74.42 \pm 1.80}$	75.72 ± 3.53	73.06 ± 3.40

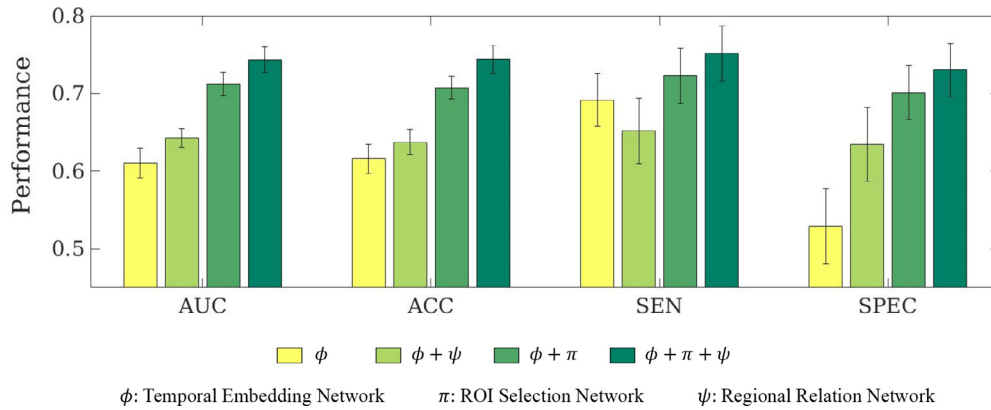**Fig. 3.** Results of our ablation study for measuring effectiveness of each network, i.e., graph convolution layer and agent.

ϕ: Temporal Embedding Network π: ROI Selection Network ψ: Regional Relation Network

Fig. 4. Visualization of feature from temporal embedding network using t-SNE. We randomly selected fold features for visualization.

using t-distributed stochastic neighbor embedding (t-SNE) (Maaten and Hinton, 2008). As depicted in Fig. 4, the groups of selected and non-selected ROIs are distinctly divided in space.

Furthermore, we investigated the correlation between selected and non-selected ROIs by randomly selecting two subjects in each group. Using the embedded features, we first reordered 114 ROIs, which were divided into selected and non-selected ROIs. We then calculated the Pearson correlation between the ROIs. As depicted in Fig. 5, the ROIs within each group, in other words, the selected ROIs group, and non-selected ROIs group show a high correlation values; whereas the inter-relation is negatively correlated. From this observation, we confirmed the agent captures selected or non-selected regional features obtained by the temporal embedding network ϕ, which are distinguishable from one another.

However, the selected ROIs do not guarantee if they are discriminatively correlated with the disease. Hence, we projected the features from the Readout function into a 2D space, using t-SNE once again. Using these features, we were able to capture the represented relations between the

selected ROIs and the discriminative information of the disease. As presented in Fig. 6, the features comprising only selected ROIs showed two clusters that are separated in the space, each of which corresponded to a group such as CN and eMCI. The selected ROIs were also found to possess valuable diagnostic information.

5.3. Reproducibility of ROIs selection and individual variability

The main role of our agent is to select ROIs individually and Fig. B1 illustrates several examples wherein ROIs are selected individually for each subject. Due to the randomness that exists in our agent network, especially in terms of episode generation, we were concerned about the reproducibility of the selected ROIs over different subjects. We repeated our experiments beyond the pretraining of networks (lines $1 - 7$ in Algorithm 1). During these repeated experiments, we recorded the agent's actions, denoted as 'action vectors' by $\{0, 1\}^{n_R}$, where n_R is the number of ROIs in a whole brain, for each of the samples in our dataset. From two independent runs (Runs #1 and #2), we compared
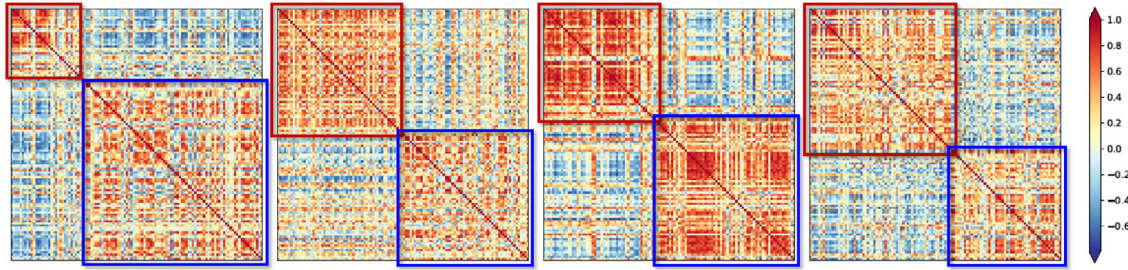
Fig. 5. Correlation matrix of embedded features. Red box and blue boxes represent selected and non-selected regions, respectively. We randomly selected four subjects and reordered the selected and non-selected ROIs. Using the feature, we calculated the Pearson correlation. Value of red color denotes a high correlation value.
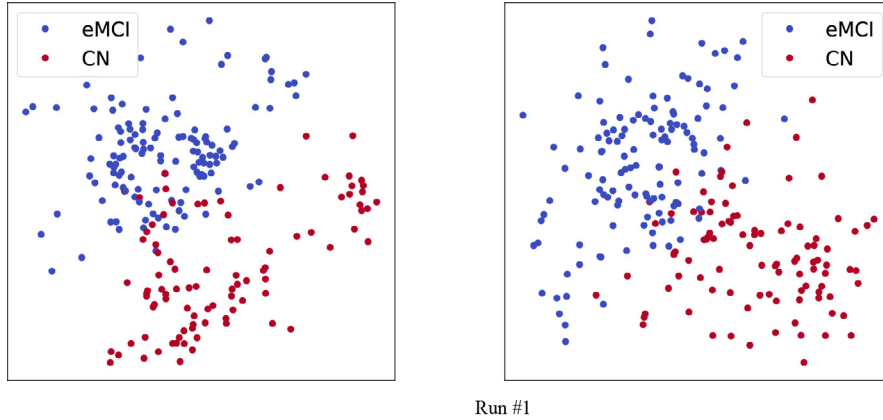

Fig. 6. Visualization of the distributions of features represented through a Readout function before the classifier using t-SNE. Each color denotes a class. Randomly selected fold features were used for visualization.
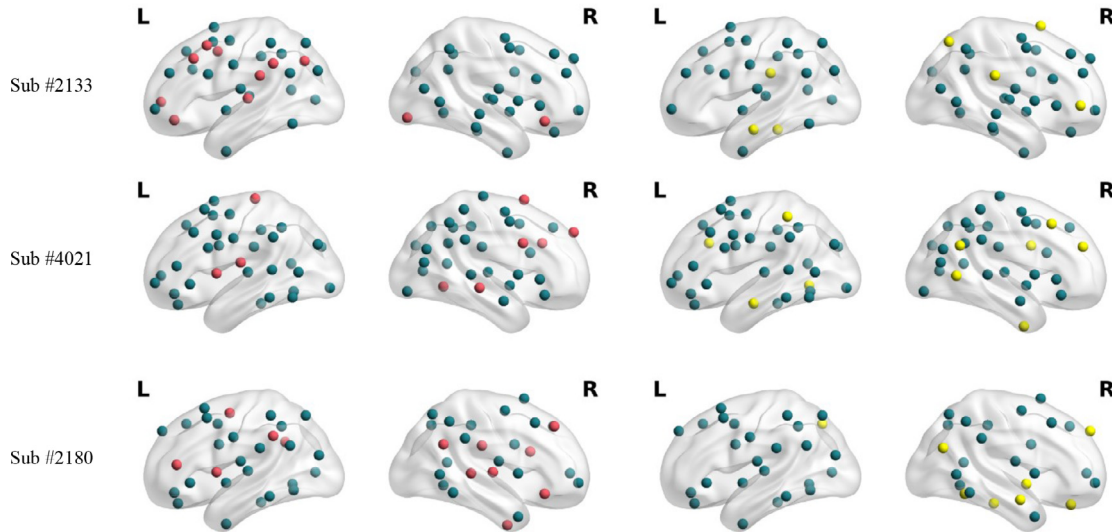

Fig. 7. Visualization of selected brain regions of randomly selected subjects. The green regions are overlapped regions between Run #1 and Run #2; red and yellow regions are from Run #1 and Run #2, respectively. Sub #n: n denotes RID in the ADNI cohort. To emphasize the regions, we removed the ROI names.

the regions that were commonly selected or not selected. Fig. 7 presents examples of three randomly chosen subjects in the dataset.

The number of overlapped regions demonstrates the reliability of our agent. For quantitative analysis, we filtered the correctly classified subjects in the test. Then, we calculated the intersection over union (IoU) by dividing the number of elements of intersection between Run #1 and Run #2 into the number of elements of union between Runs #1 and #2 (Minaee et al., 2020). We also measured the ratio of the overlapped regions with the action vectors obtained from the two runs for each sample or subject. Because the agent returns not only 1 (meaning selection) but also 0 (meaning non-selection), we calculated the IoU for the selected (IoU_1) and non-selected regions (IoU_0). From these metrics, we obtained

a mean IoU of 71.46 ± 5.71, defined as $(IoU_1 + IoU_0)/2$. The higher the mean IoU, the better the power of reproducibility of our agent network. As the mean IoU was large and the performance of our network was superior, we infer the selected ROIs, duplicated in the repeated runs, carry meaningful information regarding disease identification, and that these regions varied among the subjects, as shown in Fig. 7, reflecting individual variability.

5.4. eMCI subtype analysis

To demonstrate subject-subject variability, we conducted a subtype analysis of the eMCI group. Since the cognitive impairment has hetero-
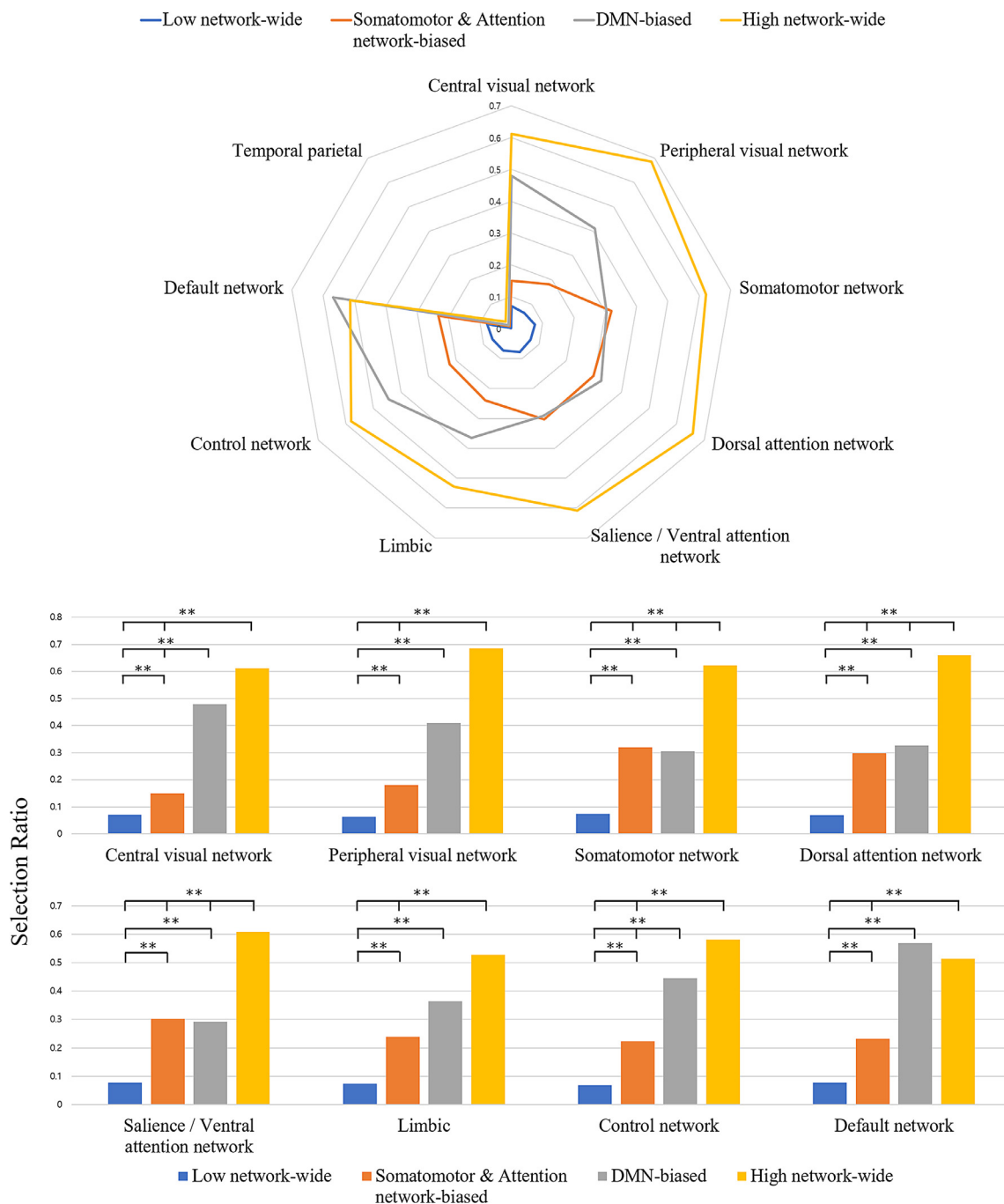
Fig. 8. Top: subtype of eMCI. Each color of line denotes each subgroup. Bottom: statistical test results for subtype analysis using selection vector from agent network. ∗∗ denotes *p* <0.005. Each color of bar plot denotes the each subgroup.

geneous manifestations that correspond to different regions or networks having different deficits, we expected that our ROI selection network, which is capable of considering individual characteristics, will also be able to effectively identify differences between the different subtypes of MCI. From the perspective of reliability, the subtype analysis will also demonstrate that our selected ROIs are not randomly inferred from the rs-fMRI signals. A hierarchical clustering using the Ward linkage method is widely used to cluster different types of input data, especially in the field of neuroimaging (Clark et al., 2013; Edmonds et al., 2019; Nettik-simmons et al., 2014). Taking the pattern of the selection vector from the agent as an input, we clustered eMCI into four subtypes. Moreover, we conducted a statistical test at the functional network level to examine the validity of these subtypes.

For the convenience of interpretation, we represented the subgroups obtained from the clustering analysis at the network level. As such, we calculated the selection ratio of the network by counting the selected ROIs in the network and dividing it by the number of ROIs belonging to the network and the number of subjects in a subgroup. According to the analysis, four subgroups were identified: (1) somatomotor and attention network-biased, (2) low network-wide, (3) DMN-biased, and (4) high network-wide group. Somatomotor and attention network-biased group mainly included the regions of the somatomotor and attention networks. The DMN-biased group showed prominently chose regions of the DMN. The low network-wide group showed the lowest selection ratio amongst all the networks, whereas the high network-wide group showed the highest selection ratio amongst all the net-
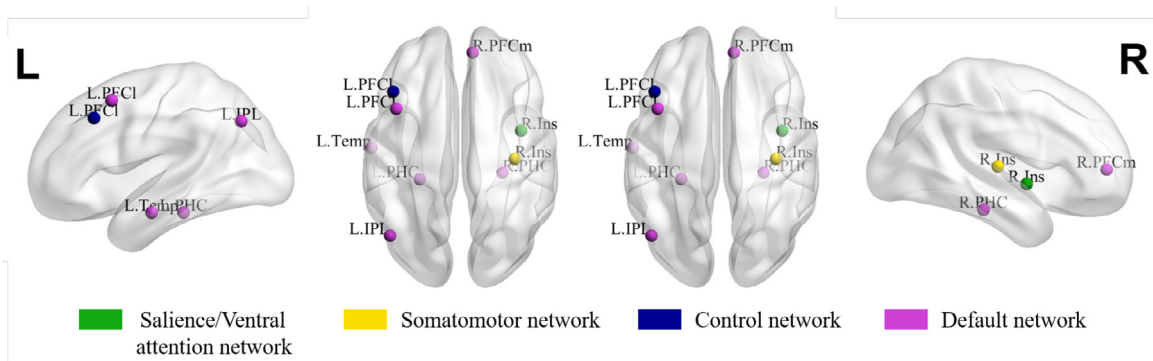
Fig. 9. Statistically different regions between CN and eMCI. The node color denotes each network.
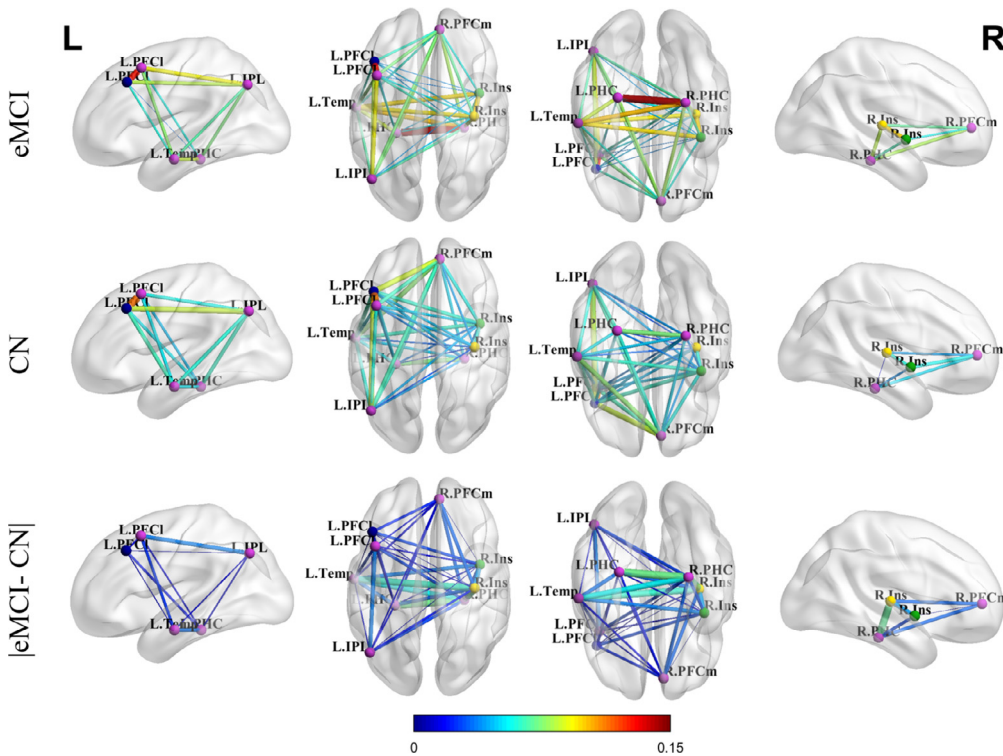

Fig. 10. Edges from the GCN of eMCI group (top), CN group (middle), and the absoluted difference between two groups (bottom). The thickness of the edges denotes the strength of the value of edge.

works. All the subgroup selection ratios are presented in Fig. 8. To validate if these subgroups differed significantly in terms of their characteristics, we conducted the Wilcoxon rank-sum test (p <0.005) using the selection ratio of each network. As shown in Fig. 8, most networks show statistically significant results in all the subgroups. Based on these results, we can conclude that our agent considered both personal and subtype properties and was unaffected by noise or randomness.

5.5. Investigation of the selected ROIs

For the neuroscientific analysis of the eMCI and CN groups at the regional level, we conducted a group analysis based on the action vectors from our agent network. We took the sum of the action vectors for all the subjects within each group, CN and eMCI; this resulted in one frequency vector per group. Then, we investigated the ROIs that showed significantly different frequency counts between the two groups, based on a Chi-square test. In Fig. 9, we visualized the significantly different regions between the groups by mapping the elements into the various regions of the brain using the BrainNet Viewer (Xia et al., 2013). The col-

ors in the figure indicate the functional networks. The regions selected[8] using by Chi-square ($p < 0.05$) are as follows:

- Somatomotor network: insula (R)
- Salience/Ventral attention network: insula (R)
- Control network: lateral prefrontal cortex (L)
- Default network: inferior parietal lobule (L), temporal (L), lateral prefrontal cortex (L), parahippocampal cortex (L), medial prefrontal cortex (R), parahippocampal cortex (R)

To be specific, with respect to the somatomotor network and the salience/ventral attention network, abnormalities in the insular, the hub of the human brain network, cognition, and sensory processing, have previously been reported in MCI subjects (Xie et al., 2012). The other regions were mostly included in the DMN; this finding coincides with those of the previous studies. The DMN is one of the most investigated networks for MCI (Eyler et al., 2019; Koch et al., 2012). The inferior parietal lobule, lateral prefrontal cortex (also the selected from control network), and medial prefrontal cortex show abnormal and impaired

---

[8] For all regions name, refer to Table 1

functional connections in both AD and MCI (Jin et al., 2012; Teipel et al., 2017; Wang et al., 2015). Since the temporal (temporal cortex or gyrus)[9] is associated with the memory system, it is widely known its abnormality is related to early pathological symptoms of AD (Dickerson and Sperling, 2008). The parahippocampal cortex shows decreased brain activity in MCI (Xi et al., 2012) and is known to be related to episodic memory. Further, impaired episodic memory caused by damage to the DMN is a clinically relevant symptom of MCI patients (Dunn et al., 2014).

We also analyzed the edge (similarity between ROIs) of statistically selected regions that comprised the graph in the GCN network. Similar to the region analysis, the difference between the eMCI and CN groups can be observed in the obtained similarity values. In Fig. 10, the strength of edge is higher in the eMCI group than that in the CN group, especially in the DMN including such as the right parahippocampal cortex, left parahippocampal cortex, and temporal cortex. Most studies (Badhwar et al., 2017) concerning AD and MCI analysis have reported the decreased functional connectivity in the DMN. However, it should be noted that we defined the edge as the similarity of the networks embedded feature, not the functional connectivity that we used for analysis. Therefore, it is not appropriate to compare our results to those in the literature. However, whether the edges from the embedded feature in the DMN of eMCI contain meaningful information can be inferred.

6. Conclusion

The combining of machine-learning techniques with rs-fMRI has been regarded as a useful tool and has been intensively investigated for the identification of degenerative brain diseases such as AD. For feature selection and/or extraction, conventional methods perform feature selection from a group perspective. In this study, we built our method by considering individual variability and accordingly defined problems for informative region selection and relational representation learning for eMCI identification. We propose a novel framework for identifying a subject with eMCI, in which the ROIs are selected automatically and individually using an RL mechanism, and their regional relations are trained using a GCN. In particular, our agent network automatically selects ROIs from the temporally embedded BOLD signals. Then, the GCN represents the regional relations based on a graph defined using only the selected regions. By systematically integrating these networks, we obtain different neurophysiological patterns of eMCI. In the experiment,

we used these patterns for eMCI identification in the public ADNI dataset and empirically demonstrated the validity of our proposed method by comparing it to competing baselines reported in the literature. In addition, we demonstrated the effects of our agent and GCN in an ablation study and analyzed the networks by visualizing the features of different layers in the proposed framework through the use of a t-SNE. Because our agent selected the ROIs individually, we performed our analysis by comparing the ROIs to those reported in neuroscience studies related to AD and MCI. The results indicated that our method can successfully select the relevant regions reported in neuroscience studies concerning AD. Owing to its advancements, it is of significant importance that studies on AD are conducted using longitudinal data, and it is desirable to extend this work in that direction in the future.

Code and data availability

All used experimental codes are available from the corresponding author upon reasonable request.

Declaration of Competing Interest

The authors declare that they have no conflict of interest.

Credit authorship contribution statement

Jiyeon Lee: Methodology, Software, Validation, Formal analysis, Investigation, Writing - original draft, Visualization. **Wonjun Ko:** Conceptualization, Methodology, Software, Validation, Formal analysis, Writing - original draft, Visualization. **Eunsong Kang:** Writing - original draft, Formal analysis, Visualization. **Heung-Il Suk:** Conceptualization, Methodology, Writing - review & editing, Supervision, Project administration, Funding acquisition.

Acknowledgements

---

[9] Refer to Thomas Yeo et al. (2011) to check the detailed brain regions.

Appendix A. Name of the ROIs in the Yeo Template

Table 1

Index and name of ROIs in the Yeo template (Thomas Yeo et al., 2011). Left and right indices in the table represent left- and right-hemispheric regions, respectively.

Index	ROI Label	Index	ROI Label
1	Striate cortex (Striate)	58	Striate cortex (Striate)
2	Extra-striate cortex (ExStr)	59	Extra-striate cortex (ExStr)
3	Striate cortex (Striate)	60	Striate cortex (Striate)
4	Extra-striate inferior (ExStrInf)	61	Extra-striate inferior (ExStrInf)
5	Extra-striate superior (ExStrSup)	62	Extra-striate superior (ExStrSup)
6	Somatomotor A (SomMotA)	63	Somatomotor A (SomMotA)
7	Central (Cent)	64	Central (Cent)
8	S2 (S2)	65	S2 (S2)
9	Insula (Ins)	66	Insula (Ins)
10	Auditory (Aud)	67	Auditory (Aud)
11	Temporal occipital (TempOcc)	68	Temporal occipital (TempOcc)
12	Parietal occipital (ParOcc)	69	Parietal occipital (ParOcc)
13	Superior parietal lobule (SPL)	70	Superior parietal lobule (SPL)
14	Temporal occipital (TempOcc)	71	Temporal occipital (TempOcc)
15	Post central (PostC)	72	Post central (PostC)
16	Frontal eye fields (FEF)	73	Frontal eye fields (FEF)
17	Precentral ventral (PrCv)	74	Precentral ventral (PrCv)
18	Parietal operculum (ParOper)	75	Parietal operculum (ParOper)
19	Precentral ventral (PrCv)	76	Precentral (PrC)
20	Insula (Ins)	77	Precentral ventral (PrCv)
21	Parietal medial (ParMed)	78	Insula (Ins)
22	Frontal medial (FrMed)	79	Parietal medial (ParMed)
23	Inferior parietal lobule (IPL)	80	Frontal medial (FrMed)
24	Dorsal prefrontal cortex (PFCd)	81	Inferior parietal lobule (IPL)
25	Lateral prefrontal cortex (PFCl)	82	Dorsal prefrontal cortex (PFCd)
26	Ventral prefrontal cortex (PFCv)	83	Lateral prefrontal cortex (PFCl)
27	Orbital frontal cortex (OFC)	84	Lateral ventral prefrontal cortex (PFClv)
28	Medial posterior prefrontal cortex (PFCmp)	85	Ventral prefrontal cortex (PFCv)
29	Temporal pole (TempPole)	86	Medial posterior prefrontal cortex (PFCmp)
30	Orbital frontal cortex (OFC)	87	Cingulate anterior (Cinga)
31	Temporal (Temp)	88	Temporal pole (TempPole)
32	Intraparietal sulcus (IPS)	89	Orbital frontal cortex (OFC)
33	Dorsal prefrontal cortex (PFCd)	90	Temporal (Temp)
34	Lateral prefrontal cortex (PFCl)	91	Intraparietal sulcus (IPS)
35	Lateral ventral prefrontal cortex (PFClv)	92	Dorsal prefrontal cortex (PFCd)
36	Cingulate anterior (Cinga)	93	Lateral prefrontal cortex (PFCl)
37	Temporal (Temp)	94	Cingulate anterior (Cinga)
38	Inferior parietal lobule (IPL)	95	Temporal (Temp)
39	Dorsal prefrontal cortex (PFCd)	96	Inferior parietal lobule (IPL)
40	Lateral prefrontal cortex (PFCl)	97	Lateral dorsal prefrontal cortex (PFCld)
41	Lateral ventral prefrontal cortex (PFClv)	98	Lateral ventral prefrontal cortex (PFClv)
42	Medial posterior prefrontal cortex (PFCmp)	99	Medial posterior prefrontal cortex (PFCmp)
43	Precuneus (pCun)	100	Precuneus (pCun)
44	Cingulate posterior (Cingp)	101	Cingulate posterior (Cingp)
45	Inferior parietal lobule (IPL)	102	Temporal (Temp)
46	Dorsal prefrontal cortex (PFCd)	103	Inferior parietal lobule (IPL)
47	Posterior cingulate cortex (PCC)	104	Dorsal prefrontal cortex (PFCd)
48	Medial prefrontal cortex (PFCm)	105	Posterior cingulate cortex (PCC)
49	Temporal (Temp)	106	Medial prefrontal cortex (PFCm)
50	Inferior parietal lobule (IPL)	107	Temporal (Temp)
51	Dorsal prefrontal cortex (PFCd)	108	Anterior temporal (AntTemp)
52	Lateral prefrontal cortex (PFCl)	109	Dorsal prefrontal cortex (PFCd)
53	Ventral prefrontal cortex (PFCv)	110	Ventral prefrontal cortex (PFCv)
54	Inferior parietal lobule (IPL)	111	Inferior parietal lobule (IPL)
55	Retrosplenial (Rsp)	112	Retrosplenial (Rsp)
56	Parahippocampal cortex (PHC)	113	Parahippocampal cortex (PHC)
57	Temporal parietal (TempPar)	114	Temporal parietal (TempPar)

Central visual network = (1-12, 58-59); Peripheral visual network = (3-5, 60-63); Somatomotor network = (6-10, 63-67); Dorsal attention network = (11-17, 68-74); Salience/ Ventral attention network = (18-28, 75-87); Limbic = (29-30, 88-89); Control network = (31-44, 90-101); Default network = (45-56, 102-113); Temporal parietal = (57, 114)

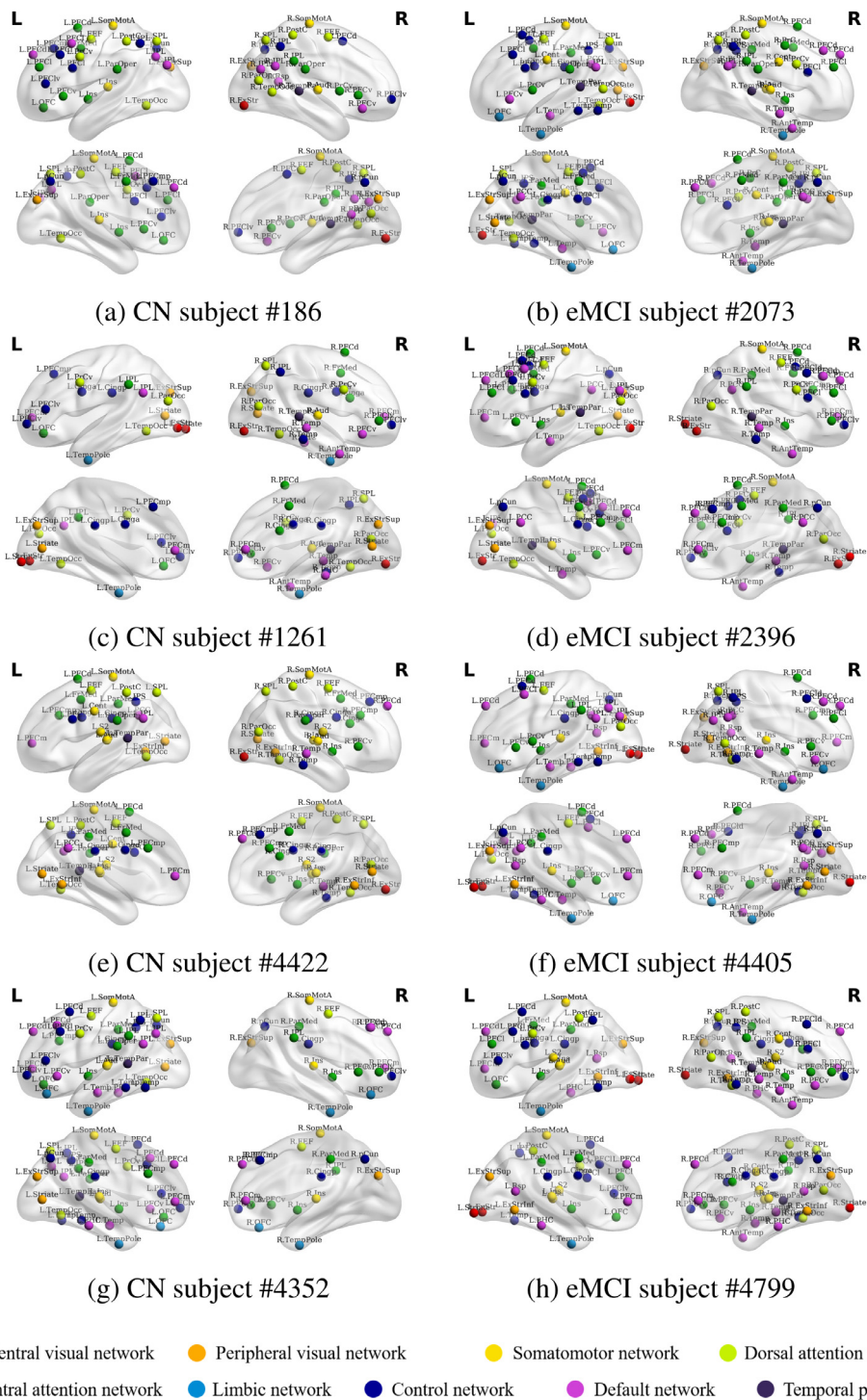**Appendix B. Visualization of selected regions of each subject**

(a) CN subject #186

(b) eMCI subject #2073

(c) CN subject #1261

(d) eMCI subject #2396

(e) CN subject #4422

(f) eMCI subject #4405

(g) CN subject #4352

(h) eMCI subject #4799

● Central visual network   ● Peripheral visual network   ● Somatomotor network   ● Dorsal attention network

● Salience/Ventral attention network   ● Limbic network   ● Control network   ● Default network   ● Temporal parietal network

Fig. B1. Visualization of the selected regions in each subject. We randomly selected four subjects from each group. Subject #*n*: *n* denotes the RID in the ADNI cohort.

Table 2

A performance comparison of comparative methods on ADNI dataset. Boldface indicates the highest value in each metric. ⋆ denotes the statistical significance in $p < 0.01$. Our proposed method (Ours) is shown significantly improved results compared to other methods.

Methods	AUC	ACC (%)	SEN (%)	SPEC (%)
SVM	$0.5511 \pm 0.1123^\star$	76.33 ± 8.75	18.54 ± 21.96	91.68 ± 7.84
CNN	$0.5388 \pm 0.1233^\star$	$55.63 \pm 11.36^\star$	59.37 ± 12.22	48.39 ± 14.07
SA-CNN	$0.5766 \pm 0.0780^\star$	78.88 ± 7.28	21.47 ± 14.40	$\mathbf{93.84 \pm 77.81}$
LSTM-DG	$0.6049 \pm 0.1141^\star$	$63.86 \pm 9.69^\star$	68.60 ± 12.25	52.39 ± 23.16
BrainNetCNN	$0.7074 \pm 0.0845^\star$	71.61 ± 8.65	75.16 ± 9.65	66.13 ± 11.39
GNN	$0.6024 \pm 0.0801^\star$	$59.59 \pm 9.77^\star$	59.18 ± 1.40	64.40 ± 13.57
GAPool	$0.5201 \pm 0.0689^\star$	$50.66 \pm 7.72^\star$	51.25 ± 12.35	50.76 ± 15.87
Ours (Bandit)	$0.6999 \pm 0.0653^\star$	71.67 ± 5.93	$\mathbf{81.72 \pm 6.93}$	58.26 ± 11.01
Ours	$\mathbf{0.7388 \pm 0.0708}$	$\mathbf{73.72 \pm 7.89}$	74.93 ± 12.65	72.85 ± 8.21

Appendix C. Additional experiments of sMCI vs. pMCI

C1. Materials and preprocessing

C1.1. ADNI cohort

We used data from 96 subjects from the ADNI cohort (in ADNI2 and ADNI GO). Specifically, we collected a dataset comprising 76 individuals with stable MCI (sMCI; 42F/34M) and 20 progressive MCI (pMCI; 10F/10M) individuals. Their mean ages were 72.2 ± 7.9 and 72.1 ± 5.96, respectively. Furthermore, the sMCI subjects have 27.99 ± 1.91 and the pMCI subjects have 25.31 ± 1.90 MMSE scores on average, respectively. Finally, CDR scores are 0.47 ± 0.16 and 0.71 ± 0.25 for the sMCI and the pMCI groups. From the longitudinal data, we obtained total 316 samples (252 sMCI and 64 pMCI). The images were scanned using 3.0T Philips Achieva scanners in multi-center with following protocol and parameters: Repetition Time (TR) = 3000ms, Echo Time (TE) = 30ms, flip angle = 80°, acquisition image size = 64×64, 48 slices, 140 time points, and a voxel thickness = 3.3mm.

C1.2. Preprocessing

We followed the same preprocessing procedure described in our main manuscript.

C2. Experiments

C2.1. Comparative methods

To demonstrate the validity of the proposed framework on the sMCI vs. pMCI diagnosis task, we exploited competing baselines used in our eMCI vs. CN diagnosis experiments, i.e., FC-SVM, CNN, SA-CNN, LSTM-DG (Dvornek et al., 2019), BrainNetCNN (Kawahara et al., 2017), GNN (Parisot et al., 2018), GAPool (Knyazev et al., 2019), and Ours (Bandit). We also calculated the four metrics: ACC, SEN, SPE, and AUC.

C2.2. Performance comparison

The entire experimental results of the sMCI vs. pMCI diagnosis task is summarized in Table 2. To be specific, the proposed framework achieved the best accuracy (73.72 ± 7.89) and AUC (0.7388 ± 0.0708), thereby demonstrating superiority over the competing baselines. To demonstrate statistical significance, we performed a Wilcoxon signed-rank test.

References

Allen, E.A., Erhardt, E.B., Damaraju, E., Gruner, W., Segall, J.M., Silva, R.F., Havlicek, M., Rachakonda, S., Fries, J., Kalyanam, R., et al., 2011. A baseline for the multivariate comparison of resting-state networks. Front. Syst. Neurosci. 5, 2.

Arbabshirani, M.R., Plis, S., Sui, J., Calhoun, V.D., 2017. Single subject prediction of brain disorders in neuroimaging: promises and pitfalls. NeuroImage 145, 137–165.

Arulkumaran, K., Deisenroth, M. P., Brundage, M., Bharath, A. A., 2017. A brief survey of deep reinforcement learning. arXiv:1708.05866.

Badhwar, A., Tam, A., Dansereau, C., Orban, P., Hoffstaedter, F., Bellec, P., 2017. Resting-state network dysfunction in Alzheimer's disease: a systematic review and meta–analysis. Alzheimer's Dement. 8, 73–85.

Calhoun, V.D., Adali, T., 2012. Multisubject independent component analysis of fMRI: a decade of intrinsic networks, default mode, and neurodiagnostic discovery. IEEE Rev. Biomed. Eng. 5, 60–73.

Cangea, C., Veličković, P., Jovanović, N., Kipf, T., Liò, P., 2018. Towards sparse hierarchical graph classifiers. arXiv:1811.01287.

Chen, X., Zhang, H., Zhang, L., Shen, C., Lee, S.-W., Shen, D., 2017. Extraction of dynamic functional connectivity from brain grey matter and white matter for MCI classification. Hum. Brain Mapp. 38 (10), 5019–5034.

Chung, F.R., Graham, F.C., 1997. Spectral Graph Theory. American Mathematical Soc..

Clark, L.R., Delano-Wood, L., Libon, D.J., McDonald, C.R., Nation, D.A., Bangen, K.J., Jak, A.J., Au, R., Salmon, D.P., Bondi, M.W., 2013. Are empirically-derived subtypes of mild cognitive impairment consistent with conventional subtypes? J. Int. Neuropsychol.Soc. 19 (6), 635–645.

Defferrard, M., Bresson, X., Vandergheynst, P., 2016. Convolutional neural networks on graphs with fast localized spectral filtering. In: Advances in Neural Information Processing Systems, pp. 3844–3852.

Delano-Wood, L., Bondi, M.W., Sacco, J., Abeles, N., Jak, A.J., Libon, D.J., Bozoki, A., 2009. Heterogeneity in mild cognitive impairment: differences in neuropsychological profile and associated white matter lesion pathology. J. Int. Neuropsychol.Soc. 15 (6), 906.

Dickerson, B.C., Sperling, R.A., 2008. Functional abnormalities of the medial temporal lobe memory system in mild cognitive impairment and Alzheimer's disease: insights from functional MRI studies. Neuropsychologia 46 (6), 1624–1635.

Dozat, T., 2016. Incorporating Nesterov momentum into Adam.

Du, Y., Fu, Z., Calhoun, V.D., 2018. Classification and prediction of brain disorders using functional connectivity: promising but challenging. Front. Neurosci. 12, 525.

Du, Y., Fu, Z., Sui, J., Gao, S., Xing, Y., Lin, D., Salman, M., Abrol, A., Rahaman, M.A., Chen, J., et al., 2020. NeuroMark: an automated and adaptive ICA based pipeline to identify reproducible fMRI markers of brain disorders. NeuroImage 28, 102375.

Dunn, C.J., Duffy, S.L., Hickie, I.B., Lagopoulos, J., Lewis, S.J., Naismith, S.L., Shine, J.M., 2014. Deficits in episodic memory retrieval reveal impaired default mode network connectivity in amnestic mild cognitive impairment. NeuroImage 4, 473–480.

Dvornek, N.C., Li, X., Zhuang, J., Duncan, J.S., 2019. Jointly discriminative and generative recurrent neural networks for learning from fMRI. In: International Workshop on Machine Learning in Medical Imaging. Springer, pp. 382–390.

Edmonds, E.C., McDonald, C.R., Marshall, A., Thomas, K.R., Eppig, J., Weigand, A.J., Delano-Wood, L., Galasko, D.R., Salmon, D.P., Bondi, M.W., et al., 2019. Early versus late MCI: improved MCI staging using a neuropsychological approach. Alzheimer's Dement. 15 (5), 699–708.

Eyler, L.T., Elman, J.A., Hatton, S.N., Gough, S., Mischel, A.K., Hagler, D.J., Franz, C.E., Docherty, A., Fennema-Notestine, C., Gillespie, N., et al., 2019. Resting state abnormalities of the default mode network in mild cognitive impairment: a systematic review and meta-analysis. J. Alzheimer's Dis. 70 (1), 107–120.

Gu, J., Wang, Z., Kuen, J., Ma, L., Shahroudy, A., Shuai, B., Liu, T., Wang, X., Wang, G., Cai, J., et al., 2018. Recent advances in convolutional neural networks. Pattern Recognit. 77, 354–377.

Hosseini-Asl, E., Gimel'farb, G., El-Baz, A., 2016. Alzheimer's disease diagnostics by a deeply supervised adaptable 3D convolutional network. arXiv:1607.00556.

Jin, M., Pelak, V.S., Cordes, D., 2012. Aberrant default mode network in subjects with amnestic mild cognitive impairment using resting-state functional MRI. Magn. Reson. Imaging 30 (1), 48–61.

Kawahara, J., Brown, C.J., Miller, S.P., Booth, B.G., Chau, V., Grunau, R.E., Zwicker, J.G., Hamarneh, G., 2017. BrainNetCNN: convolutional neural networks for brain networks; towards predicting neurodevelopment. NeuroImage 146, 1038–1049.

Khazaee, A., Ebrahimzadeh, A., Babajani-Feremi, A., Initiative, A.D.N., et al., 2017. Classification of patients with MCI and AD from healthy controls using directed graph measures of resting-state fMRI. Behav. Brain Res. 322, 339–350.

Kipf, T. N., Welling, M., 2016. Semi-supervised classification with graph convolutional networks. arXiv:1609.02907.

Knyazev, B., Taylor, G.W., Amer, M., 2019. Understanding attention and generalization in graph neural networks. In: Advances in Neural Information Processing Systems, pp. 4204–4214.

Koch, W., Teipel, S., Mueller, S., Benninghoff, J., Wagner, M., Bokde, A.L., Hampel, H., Coates, U., Reiser, M., Meindl, T., 2012. Diagnostic power of default mode network

resting state fMRI in the detection of Alzheimer's disease. Neurobiol. Aging 33 (3), 466–478.

Ktena, S.I., Parisot, S., Ferrante, E., Rajchl, M., Lee, M., Glocker, B., Rueckert, D., 2018. Metric learning with spectral graph convolutions on brain connectivity networks. NeuroImage 169, 431–442.

Maaten, L.v.d., Hinton, G., 2008. Visualizing data using t-SNE. J. Mach. Learn. Res. 9 (Nov), 2579–2605.

Medaglia, J.D., 2017. Graph theoretic analysis of resting state functional MR imaging. Neuroimaging 27 (4), 593–607.

Minaee, S., Boykov, Y., Porikli, F., Plaza, A., Kehtarnavaz, N., Terzopoulos, D., 2020. Image segmentation using deep learning: a survey. arXiv:2001.05566.

Mohr, P.N., Nagel, I.E., 2010. Variability in brain activity as an individual difference measure in neuroscience? J. Neurosci. 30 (23), 7755–7757.

Mueller, S., Wang, D., Fox, M.D., Yeo, B.T., Sepulcre, J., Sabuncu, M.R., Shafee, R., Lu, J., Liu, H., 2013. Individual variability in functional connectivity architecture of the human brain. Neuron 77 (3), 586–595.

Nettiksimmons, J., DeCarli, C., Landau, S., Beckett, L., Initiative, A.D.N., et al., 2014. Biological heterogeneity in ADNI amnestic mild cognitive impairment. Alzheimer's Dement. 10 (5), 511–521.

Parisot, S., Ktena, S.I., Ferrante, E., Lee, M., Guerrero, R., Glocker, B., Rueckert, D., 2018. Disease prediction using graph convolutional networks: application to autism spectrum disorder and Alzheimers disease. Med. Image Anal. 48, 117–130.

Qian, L., Zheng, L., Shang, Y., Zhang, Y., Zhang, Y., disease Neuroimaging Initiative, A., et al., 2018. Intrinsic frequency specific brain networks for identification of MCI individuals using resting-state fMRI. Neurosci. Lett. 664, 7–14.

Rathore, S., Habes, M., Iftikhar, M.A., Shacklett, A., Davatzikos, C., 2017. A review on neuroimaging-based classification studies and associated feature extraction methods for Alzheimer's disease and its prodromal stages. NeuroImage 155, 530–548.

Shen, D., Wu, G., Suk, H.-I., 2017. Deep Learning in Medical Image Analysis. Annu. Rev. Biomed. Eng. 19, 221–248.

Sohn, W.S., Yoo, K., Lee, Y.-B., Seo, S.W., Na, D.L., Jeong, Y., 2015. Influence of ROI selection on resting state functional connectivity: an individualized approach for resting state fMRI analysis. Front. Neurosci. 9, 280.

Sutton, R., Barto, A., 2018. Reinforcement Learning: an Introduction. MIT Press.

Sutton, R.S., McAllester, D.A., Singh, S.P., Mansour, Y., 2000. Policy gradient methods for reinforcement learning with function approximation. In: Advances in Neural Information Processing Systems, pp. 1057–1063.

Szegedy, C., Vanhoucke, V., Ioffe, S., Shlens, J., Wojna, Z., 2016. Rethinking the inception architecture for computer vision. In: Proceedings of the IEEE Conference on Computer Vision and Pattern Recognition, pp. 2818–2826.

Teipel, S.J., Wohlert, A., Metzger, C., Grimmer, T., Sorg, C., Ewers, M., Meisenzahl, E., Klöppel, S., Borchardt, V., Grothe, M.J., et al., 2017. Multicenter stability of resting state fMRI in the detection of Alzheimer's disease and amnestic MCI. NeuroImage 14, 183–194.

Thomas Yeo, B., Krienen, F.M., Sepulcre, J., Sabuncu, M.R., Lashkari, D., Hollinshead, M., Roffman, J.L., Smoller, J.W., Zöllei, L., Polimeni, J.R., et al., 2011. The organization of the human cerebral cortex estimated by intrinsic functional connectivity. J. Neurophysiol. 106 (3), 1125–1165.

Vaswani, A., Shazeer, N., Parmar, N., Uszkoreit, J., Jones, L., Gomez, A. N., Kaiser, L., Polosukhin, I., 2017. Attention is all you need. arXiv:1706.03762.

Wang, J., Zuo, X., He, Y., 2010. Graph-based network analysis of resting-state functional MRI. Front. Syst. Neurosci. 4, 16.

Wang, L., Lei, Y., Zeng, Y., Tong, L., Yan, B., 2013. Principal feature analysis: a multivariate feature selection method for FMRI data. Computat. Math. Methods Med. 2013.

Wang, Z., Xia, M., Dai, Z., Liang, X., Song, H., He, Y., Li, K., 2015. Differentially disrupted functional connectivity of the subregions of the inferior parietal lobule in Alzheimers disease. Brain Structure and Function 220 (2), 745–762.

Wee, C.-Y., Yap, P.-T., Zhang, D., Wang, L., Shen, D., 2014. Group-constrained sparse fMRI connectivity modeling for mild cognitive impairment identification. Brain Struct. Funct. 219 (2), 641–656.

Xi, Q., Zhao, X., Wang, P., Guo, Q., Jiang, H., Cao, X., He, Y., Yan, C., 2012. Spontaneous brain activity in mild cognitive impairment revealed by amplitude of low-frequency fluctuation analysis: a resting-state fMRI study. La Radiol. Med. 117 (5), 865–871.

Xia, M., Wang, J., He, Y., 2013. BrainNet Viewer: a network visualization tool for human brain connectomics. PLoS One 8 (7).

Xie, C., Bai, F., Yu, H., Shi, Y., Yuan, Y., Chen, G., Li, W., Chen, G., Zhang, Z., Li, S.-J., 2012. Abnormal insula functional network is associated with episodic memory decline in amnestic mild cognitive impairment. NeuroImage 63 (1), 320–327.

Xu, K., Hu, W., Leskovec, J., Jegelka, S., 2018. How powerful are graph neural networks? arXiv:1810.00826.

Yan, C.-G., Wang, X.-D., Zuo, X.-N., Zang, Y.-F., 2016. DPABI: data processing & analysis for (resting-state) brain imaging. Neuroinformatics 14 (3), 339–351.

Yan, Y., Zhu, J., Duda, M., Solarz, E., Sripada, C., Koutra, D., 2019. Groupinn: grouping-based interpretable neural network for classification of limited, noisy brain data. In: Proceedings of the 25th ACM SIGKDD International Conference on Knowledge Discovery & Data Mining, pp. 772–782.

Zaheer, M., Kottur, S., Ravanbakhsh, S., Poczos, B., Salakhutdinov, R.R., Smola, A.J., 2017. Deep sets. In: Advances in Neural Information Processing Systems, pp. 3391–3401.

Zou, H., Hastie, T., 2005. Regularization and variable selection via the elastic net. J. R. Stat. Soc. 67 (2), 301–320.